

Measurement and Computation Techniques for 8-D reflectance field

SEIICHI TAGAWA^{1,a)} YASUHIRO MUKAIGAWA¹ YASUSHI YAGI¹

Abstract: The appearance of an object depends on its photometric properties: the reflectance, illumination, and observation. Of the three factors that control appearance, reflectance is the most difficult to deal with and control. An eight-dimensional reflectance field can completely represent an appearance consisting of the reflectances of objects, illumination, observation, and interreflections between objects. However, because of the high dimensionality, 8-D reflectance fields have not been developed sufficiently. To realize practical use of an 8-D reflectance field, we developed a polyhedral mirror named the turtleback reflector that can measure entire 8-D reflectance fields, proposed a computing method that can generalize some computational photography techniques, and an analyzing methods named hemispherical confocal imaging that can clearly visualize a particular depth of a target scene by an 8-D reflectance field measuring system.

1. Introduction

People post many photos on the internet of things that fascinate us. Almost all of them use digital cameras to capture such scenes. Because recent digital cameras have megapixel resolution, a captured image can provide us with details of the target scene. However, the appearances of the scenes change with the focus, viewpoint, and lighting, which cannot be changed once the images are captured. That is because an image has just two-dimensional information.

The image represents information from the rays that reached a camera lens. When the lens gathers rays from the object focal point, the rays are refracted and converge at a sensor at the image focal point. Here, the information of every ray is collapsed into one pixel intensity, where the variation of each ray angle is lost in the captured image. In a lens, the focal plane is changed by changing the variation of the gathered ray angles. So, if we have all of the ray information for every angle, we can produce an image when focusing at an arbitrary depth.

The ray information is provided by the illumination of the scene from surrounding light sources. When the illumination varies, the ray information consisting of reflected light from the scene also varies. Hence, to store appearances of the scene, we should measure all information in every reflected illumination ray.

1.1 Computational Photography

To acquire more information about a scene than just an image, we should know how information is lost in capturing an image by camera. Also, we should consider how to maintain, at least, the important information in captured rays for specific applications.

The digital camera has evolved so that we can store a beautiful scene in a vivid image with high-resolution sensors and digital image processing. However, the scheme of capturing has not changed except for replacement of sensitive films with digital sensors. Present cameras use a conventional lens, diaphragm, and flash to capture images. Hence, because the process of maintaining information has not changed, much information has been collapsed.

Recently, many researchers have been interested in changing this scheme. In computational photography, the lens aperture has been coded to make all-in-focus images [16]. The exposure time has also been coded to deblur images that capture moving objects [32]. Although conventional cameras do not always need image processing to provide us with an image, novel cameras often need image processing to provide us with an excellent image. This way, computational photography can create great effects in an image using computation-based optics.

So far, photography has been about integrating ray intensities from a scene. The lighting is used only for flash. However, because illumination conditions change appearances, sophisticated illumination can add novel features to photography. For example, Kim et al. [12] have proposed a simple but very interesting technique. In highlighted depth-of-field photography, a projector projects and focuses a pattern onto the target object. Here, the patterns on the other objects are blurred. Kim et al. [12] analyzed the focused pattern to brighten the target object and darken the other objects. So, they used a projector as sophisticated illumination and successfully emphasized the target object.

In brief, the purpose of computational photography is to maintain important properties of a scene in a captured image via specially designed optics. Camera optics and scene illumination have been designed to achieve this. Here, it is important to understand what property can be included in a captured image.

¹ Osaka University

^{a)} tagawa@am.sanken.osaka-u.ac.jp

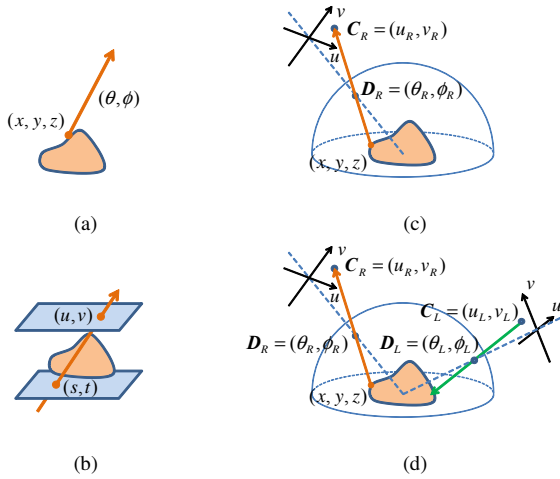


Fig. 1 Descriptions of the light and reflectance fields. Both illumination and reflection can be described as a 4DLF. Hence the combination can be represented as an 8DRF.

1.2 8-Dimensional Reflectance Field

An image captured by a camera represents an appearance of a scene under specific conditions. What we can acquire from images is determined by the limitation of the finest appearance information.

The appearances of an object or a scene depend on how the light is reflected at the surface. If we want to control the appearance freely, we need all of the properties of the scene. So, in computer graphics great effort has been made to create realistic images of synthetic objects that do not really exist. To do this, many researchers have addressed how to measure the property, how to model the property, how to image the property, and how to deal with the interreflection. However, if we want to control the appearances of real objects under arbitrary illumination, we can do it using reflectance fields of the scene. This is called an image-based technique: image-based rendering, and image-based relighting.

The image of a scene varies when the viewpoint or the illumination changes. It is well known that an appearance can be perfectly represented by a set of rays.

First, we consider rays reflected from the scene. A ray can be expressed by the passing point (x, y, z) in the direction (θ, ϕ) as shown in **Fig. 1** (a). Hence, the intensity of the ray can be defined by five parameters. This description of the rays is called the *light field*. Here, assuming the ray is not attenuated, the intensity of the ray can be defined by four parameters, (s, t) and (u, v) , on two planes as shown in Fig. 1 (b). While this is a standard representation, it cannot describe rays that are parallel to the two planes. Hence, in this research we define the light field using a hemisphere that covers the scene as shown in Fig. 1 (c). The ray is denoted by its position on the hemisphere $D_R = (\theta_R, \phi_R)$ and its direction $C_R = (u_R, v_R)$. This is a four-dimensional light field (4DLF) denoted by $F_R(D_R, C_R)$, which can represent all the rays reflected from the scene.

Similarly, the illumination on the scene is also described as a light field. As shown in Fig. 1 (d), the incident ray can be defined by its position on the hemisphere $D_L = (\theta_L, \phi_L)$ and its direction $C_L = (u_L, v_L)$. Hence, we can denote the 4DLF of the illumination

by $F_L(D_L, C_L)$.

The relationship between the 4DLF of the illumination F_L and the 4DLF of the reflection F_R is called the *reflectance field*. Hence, we can denote the reflectance field with eight parameters by

$$F(D_L, C_L, D_R, C_R), \tag{1}$$

consisting of the two 4DLFs of illumination and reflection. This eight-dimensional reflectance field (8DRF) can perfectly describe the image of the scene from arbitrary viewpoints under arbitrary illumination conditions.

1.3 Computational Photography based on 8-Dimensional Reflectance Field

If the 8-D reflectance fields can be measured and computed, we can realize various applications, exploiting the information by controlling the illumination and observation.

The quality of industrial and consumer products should be assessed with appearances of high accuracy. We should understand how product appearances vary with every viewing angle under various lighting conditions. The 8-D reflectance field can completely represent the appearances. Further, to guarantee processing accuracy, the appearance information can give clues to detect product flaws. That is because even microscopic flaws and bumps on the surface of the target object reflect its appearance like a Chinese magic mirror, which looks like a planar mirror but actually has slight bumps on the surface that reflect sunlight toward a planar wall with a pattern that depends on the bumps. Hence, if the difference in appearance between products with and without flaws could be measured, a flaw could be detected and quantitatively verified.

Similarly, appearances could be stored accurately and in high detail for archiving objects of cultural heritage. If they have been measured, the appearances can be reproduced for any observation conditions and shown to people who cannot go to the places where the objects are displayed. Because the appearance depends on the reflectance properties of the target materials, we should store information on the reflectance properties by measuring the materials in detail.

However, no application techniques have been developed that use the 8-D reflectance field. So, we have developed the measuring device and computing framework for an 8DRF, and will apply it to an example.

Contribution

- We designed a measuring device for 8DRFs which exploits conic curve characteristics. Hence, designing the measuring devices becomes easy.
- We established a computational framework that uniformly expresses some computational photography that relates light fields and reflectance fields. With this, The relationships among presented techniques become clear.
- We showed that the usefulness of measuring 8-D reflectance field on a hemisphere by proposing a novel imaging technique that clearly capture an occluded and attenuated surface texture.

- We showed that the high dimensionality is very useful by the proposed device and application even if the resolution is quite low because of a trade-off between the measuring resolution and dimension when using a mirror system like the turtleback reflector that has many planar mirrors.

2. Related Work

Every objects have reflectance properties dependent on the microscopic shape and the opacity of the material surface. The reflectance properties can be used for various applications, for example, creating realistic computer graphics or inspections of painted surfaces. So far, various measurement systems have been developed. Li et al. [20] have developed the gonioreflectometer which is a straightforward device to measure BRDFs by rotating the sensor and light source around the target material. Systems using concave mirrors [5], [41] have developed to speed-up the measurements where the mirrors gather reflected light from a target point on the material surface. However, to measure fine reflectance properties, it takes tremendously long time because the measurement system must illuminate the target point in all directions individually, and measure the reflected light in all directions for each illumination, especially for systems with mechanical drives.

Recently, to measure fine reflectance properties rapidly, the systems combining a projector with a concave mirror. Mukaigawa et al. [24] use an ellipsoidal mirror, and Ghosh et al. [10] use an originally designed mirror. In these systems the mechanical drive to change illumination directions is replaced with the projector that changes the illumination directions by changing projected patterns rapidly. Moreover, by the concave mirror, a camera can capture all of the reflected light at once.

Generally, the scene is not a point but a 3-D scene and every point emits light in various directions. There are many researches dealing with a light field that represent light reflected from the scene. A light field is a 4-D slice of the 8-D reflectance field under static illumination. It can be recorded by a scanning camera [19] or installing many cameras [39]. Alternatively, a high-resolution camera can be combined with a micro lens array [1], a micro mirror array [37], or masks [40]. To vary the illumination, Debevec et al. [6] rotated the light source, and Sen et al. [34] used a projector as the light source. Masselus et al. [21] rotated the projector, and Matusik et al. [22] rotated both the light source and the camera to measure a 6-D reflectance field. Müller et al. [26] used 151 cameras with flashes.

In principle, the complete 8-D reflectance field can be measured by installing many projectors and cameras densely on a hemisphere. However, it is difficult to realize such a system because of the cost and the physical interference between the devices. While a rotating projector and camera solves these problems, the capture process is impractically long. Recently, Garg et al. [9] and Levoy et al. [18] used multiple planar mirrors and Cossairt et al. [4] used a lens array to measure a part of the 8-D reflectance field, but the direction of the illumination and observation was limited to a narrow angle.

An advantage of using a projector as a light source is that multiplexing techniques can be applied to illumination methods be-

cause the projector can generate light sources in various directions simultaneously.

Mukaigawa et al. [25] has multiplexed the projected patterns with the Hadamard transform and improved the S/N ratio of reflectance property measurements. It has been shown that the measurement time has been reduced by orthogonal transforms of illumination distributions on the projected patterns, Ghosh et al. [10] and Sato et al. [33] used the spherical harmonics, and Peers et al. [30] used the wavelet transform. However, although the Hadamard transform can improve the S/N ratio, it cannot reduce the measurement time. On the other hand, the techniques using the spherical harmonics or the wavelet transform can reduce the measurement time but cannot measure the proper reflectance property. If such compression techniques are used, the high frequency components of the reflected light from smooth surfaces cannot be kept because the transforms restrict the measured components to the low frequency components.

Sen et al. [34] showed that the measurement time is reduced without loss when the reflected lights of multiplexed illumination are not overlapped, in confirmation of their Dual Photography technique, which exploit the Helmholtz reciprocity to interchange the lights and cameras. However, it cannot be applied to measurements of reflectance properties because the target point is the same for every illumination and the reflected light is always overlapped.

Recently, the compressive sensing [2], [3], [7] has been well known as a useful technique to reduce the measurement time. The technique exploits data-sparseness in target information. The data-sparseness means that the information signal can be well compressed by compression transforms like the Fourier transform, and many coefficients are zero. Here, the number of non-zero coefficient is the length of minimum signal representing the information. So, when one entry of the signal is measured at one time, the measurement time can be reduced by the compressive sensing.

For measurements of reflectance fields, Peers et al. [31] have shown that the compressive sensing can be applied to the measurement of light transport, which is a six-dimensional reflectance field consisting of two-dimensional reflection under four-dimensional illumination. They have reduced the measurement time by the compressive light transport sensing, exploiting the sparseness in the light transport matrix.

Once the reflectance field is measured, we can control the depth of field of a image. Many researchers have developed photography techniques to clearly capture a scene with various DOFs which covers their targets. To shrink a DOF, they used a camera array or a lenslet array. To extend a DOF, they used coded apertures analyzed in the frequency domain.

The synthetic aperture imaging virtually creates a larger aperture having a shallow DOF. Also the imaging technique can change the depth of the focal plane after capturing the scene, well-known as the refocusing technique. Vaish et al. [39] developed a dense camera array to do it. Ng et al. [29] developed a hand-held plenoptic camera within a lenslet array. Recently, a light field camera is commercially available. Levin et al. [17] develop the lattice-focal lens consisting of parts of different focal lenses to

keep high frequency information in the wider DOF than the DOF of each single lens.

Often, a DOF of a SLR camera is too shallow to capture whole a region of interest in a target scene. So, researchers have developed methods extending a DOF using coded apertures. The coded aperture can convolve a coded PSF into a captured image. This can leave the high frequency component of the captured scene in the captured image. Therefore, an image clearly focused on whole the scene can be restored.

There are imaging techniques exploiting bokeh as an aesthetic effect. By controlling bokeh, impressive effect is given to photos. Lanman et al. [15] analyzed the spatially-varying point spread function to control bokeh. Kusumoto et al. [14] controlled defocus in the synthetic aperture imaging by an image interpolation of uncalibrated multiview images.

Reflectance fields can be analyzed to create a novel image that cannot be captured by a conventional camera. When a target object is in murky liquids or translucent media, incident light and light reflected on the object scatters and the appearance becomes blurred. In this case, if we use a conventional camera, we get an unclear view. To obtain a clear view, descattering methods are needed. Treibitz and Schechner [36] used a polarizer under water. Kim et al. [13] used a lenslet array. Assuming optically thin media, Narasimhan et al. [27] estimated a 3-D shape with descattering and Gu et al. [11] estimated the 3-D distribution of inhomogeneous scattering media.

Recently, Fuchs et al. [8] combined confocal imaging with descattering, which captured a descattered image at a particular depth in a 3-D scene. This technique consisted of the synthetic aperture confocal imaging proposed by Levoy et al. [18] and the high frequency illumination proposed by Nayar et al. [28].

3. Measuring Device for 8-D Reflectance Field

To measure 8DRFs, a target scene needed to be illuminated in every direction at every point on a hemisphere. Similarly all the reflected light needed to be measured.

To generate illumination in various directions passing through a point on a hemisphere, we can use a projector, that can be considered as a generator of two-dimensional light fields. If many projectors are densely placed on a hemisphere, the total system can be considered as a generator of four-dimensional light fields. On the other hand, a camera can capture the rays passing through the center point of the camera in various directions. Thus, a camera can be considered as a measurement device of two-dimensional light field. If many cameras are densely placed on a hemisphere, the total camera system can be considered as a measurement device of four-dimensional light field. Therefore, to develop a system that can measure 8DRFs is to place many projectors and cameras on a hemisphere densely.

3.1 Problems on Measurement

There are two major problems to measure an 8-D reflectance field.

How to Sample 8-D Reflectance Field

The simplest way to measure 8-D reflectance fields is to move a projector and camera on a hemisphere, capturing a target scene il-

luminated by the projector with all possible patterns. However, it is unrealistic for some reasons. First, a 8-D Reflectance Field will be a tremendously large data because of the high dimensionality. Second, such a measurement takes extremely large time costs. So, because it is infeasible that a whole 8-D reflectance field cannot be completely measured, we have to adequately sample it, where all the dimensions are treated uniformly.

How to Locate Optical Devices

Another problem is how to locate projectors and cameras. Simply, the projectors and cameras can be placed on a hemisphere if the distribution can be sparse. However, if the distribution of projectors and cameras must be dense, it is difficult to place them on a hemisphere because of the physical conflicts of the bodies.

3.2 Mirror Systems to Measure Reflectance Field

A mirror can translate a point passed through by a ray to the mirrored point. Hence, developing a measurement system can be considered as placement of mirrors in order to make the mirrored point at an arbitrary position on a hemisphere. Using mirrors, development of a measuring system becomes easier because arranging many mirrors is easier than arranging many projectors and cameras.

Mirror Designs via Conic Curves

Conic curves are well known as curvatures with focal points. For a curved line with focal points, a mirror along the line gathers rays at the focal point. Conic curves can be classified into four types: circle, ellipse, parabola, and hyperbola. Here, the target scene is three-dimensional, not two-dimensional. So, a three-dimensional curved surfaces are needed and they are a sphere, ellipsoid, paraboloid, and hyperboloid, respectively. Here, for simplicity, we describe about the lines not the surfaces and about arrangements of cameras. Note that designs for cameras can be applied to arrangements of projectors in the same way. In this section, we explain how to use the conic curves to arrange mirrored points on a hemisphere.

When mirrors are arranged along a circle, we can exploit characteristics of the circle, where rays passing through the center are reflected at the curve and passes through the center again. Here, the total path length is always twice of the radius. So, the mirrored point is created on a circle with twice radius. To exploit this, a camera and a target scene are needed to be placed at the center of circle. It is physically impossible. However, it is possible optically using beam splitters can be used as shown in Fig. 2 (a).

When mirrors are arranged along an ellipse, the ray passing through one focal plane is reflected on the mirror and reach the other focal point. Here, the total path lengths are always constant. Hence, placing a camera at one focal point and a target scene at the other focal point, a virtual camera is created on a circle, as shown in Fig. 2 (b).

When mirrors are arranged along a parabola, characteristics of a parabola can be exploited. Distances from a point on a parabola between to a directrix and a focal point is always the same. Therefore, when a camera is placed along the directrix, a virtual camera is placed on a circle that has the center at the focal point of the parabola, as shown in Fig. 2 (c).

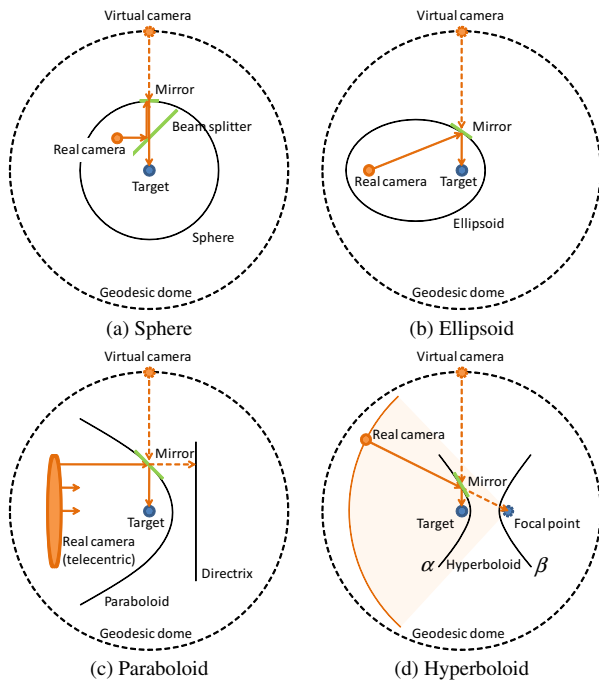


Fig. 2 Design of mirrors using conic curved surfaces.

When mirrors are arranged along a hyperbola, characteristics of hyperbola can be exploited as shown in Fig. 2 (d). In a hyperbola, there are two focal points and two curved line, a differential length between from two focal points to a point on a line is always constant. Here, a ray going to one focal point is reflected at the curved line α and goes to the other focal point. Hence, in order to let a target scene be placed at one focal point, where mirrored points created on a circle, surrounding the scene, the incident points are needed to be placed on a circle centered at the other focal point. So, the hyperbola cannot be used because such a setting assumes the purpose condition is already satisfied, where a point is surrounded by points on a circle.

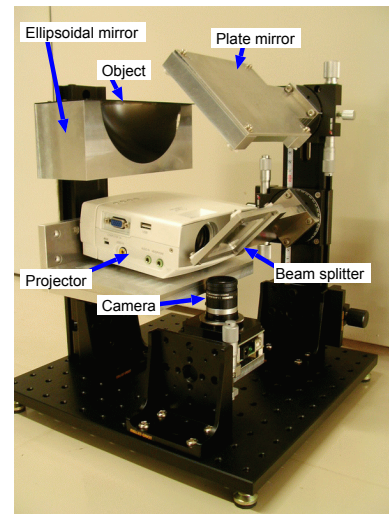
3.3 Ellipsoidal Mirror to Measure 4-D Reflectance Field

Using a conically curved mirror, we can let illuminating rays from a projector and viewing rays of a camera at a focal point be focused at the other focal point. When we need high resolution for angular variation to the target point, the curved mirror can help to measure such a reflectance property. An advantage of this kind of mirrors is the ability to transform central projection into converging projection. This way, pixels of a projector and camera which look at different points can look at the same point in various directions.

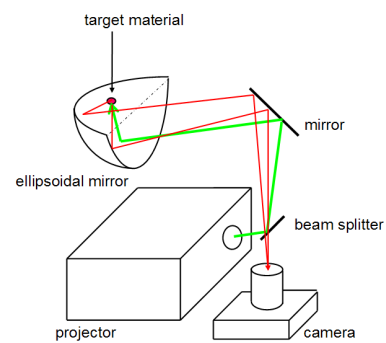
Mukaigawa et al. [24], [25] have developed a measuring system named RCG2 with an ellipsoidal mirror, as shown in Fig. 3 (a), to rapidly and finely measure BRDFs. As shown in Fig. 3 (b), using a beam splitter, a projector and camera are placed at the same focal point of an ellipsoid. So, in this system, a target point on a surface of target materials can be illuminated and observed in various directions at the same time by change of projected patterns.

3.4 Turtleback Reflector to Measure 8-D Reflectance Field

To generate and capture 4-D light fields for a 3-D scene, pro-



(a) Overview



(b) Path of ray

Fig. 3 BRDF measuring device. [25]

jectors and cameras should be placed uniformly on a hemisphere. Here, the curved mirror cannot be used because they focus all rays at a single point though the target scene is not a point but a space.

To realize this, we used planar mirrors. By combining a projector and camera with many planar mirrors, a number of virtual projectors and cameras with low resolution can be generated and can capture the scene in various directions.

Views from the virtual cameras are created in a view from the real camera. Hence, the region for each virtual camera must be cropped and warped to get virtual viewpoint images. Geometric calibration of the virtual cameras is performed by finding corresponding points in a captured image using the real camera. The geometric conversion from the real camera to virtual cameras can be achieved using simple homography. The pixel intensities of the virtual image are resampled from the captured image.

To measure 8DRFs, the planar mirrors should be properly positioned, so that they place virtual cameras on a hemisphere. A distance between the target and each virtual camera should be constant. To do this, as mentioned above, conic curves can be exploited. Practically, the designs by an ellipse and a parabola are useful. These designs are suitable for different projection systems.

For a perspective projection, the planar mirrors should be located along an ellipsoid as shown in Fig. 2 (b). On the other hand, if the projection is orthographic, the planar mirrors should be lo-

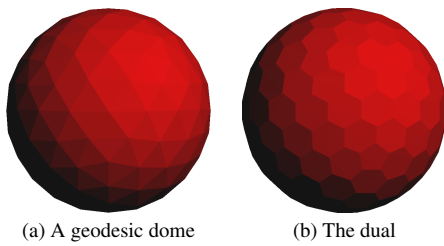


Fig. 4 Geodesic domes.

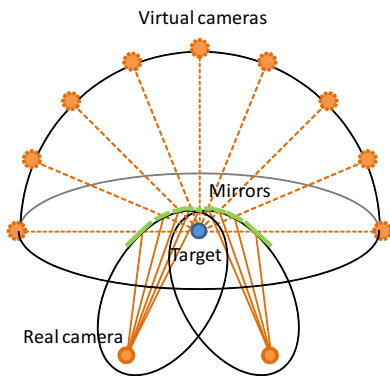


Fig. 5 Design of polyhedral mirrors using two ellipsoids.

cated along a paraboloid as shown in Fig. 2 (c).

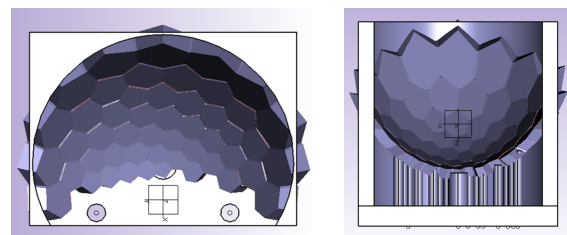
In the design using a paraboloid, a telecentric lens is needed. However, the telecentric lens is expensive. Hence, we adopted the design using an ellipsoid because it just requires a conventional lens.

In practice, the number of virtual cameras is finite. Cameras are discretely placed on a hemisphere. To measure 8DRFs, the virtual cameras should be placed with as uniform a density as possible.

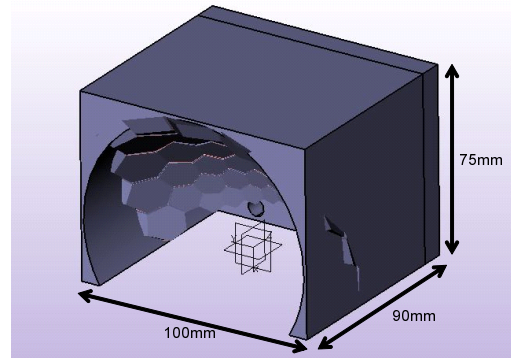
As shown in Fig. 4 (a), a geodesic dome is a well-known polyhedron that uniformly samples a sphere. The virtual cameras are located on the facets of the geodesic dome. The mirrors are located on tangent planes on the ellipsoid. The tangent point is given by the projection of the center of the facet from the center of the dome. To decide the mirror shape, the vertices of the facet are projected onto the tangent plane. These mirrors become the polyhedral mirrors, which place virtual cameras on a hemisphere with uniform density.

Each facet of the polyhedron acts as a viewing window corresponding to the virtual camera. A region commonly observed from all virtual cameras is defined by a logical AND of all the views of the virtual camera. That is, the shape of a facet should be close to a circle in order to observe a large area. Therefore, we used the dual geodesic dome shown in Fig. 4 (b) instead of the original geodesic dome, because the dual dome has pentagonal and hexagonal facets, while the original geodesic dome had triangular facets.

We now show an implementation of our polyhedral mirror. We first decided on the number of mirrors. The geodesic dome is made by dividing 20 facets of an icosahedron into 20×4^k ($k \in \mathbf{N}$) facets. The number of facets of the dual dome is then $N = 10 \times 4^k + 2$. We set $k = 2$ and $N = 162$. The upper half hemisphere consists of 81 facets. However, 81 facets do not completely cover the upper hemisphere. Hence we added 10 horizon-



(a) front view (b) bottom view



(c) dimensions

Fig. 6 Design of the frame for the turtleback reflector.



Fig. 7 Turtleback reflector.

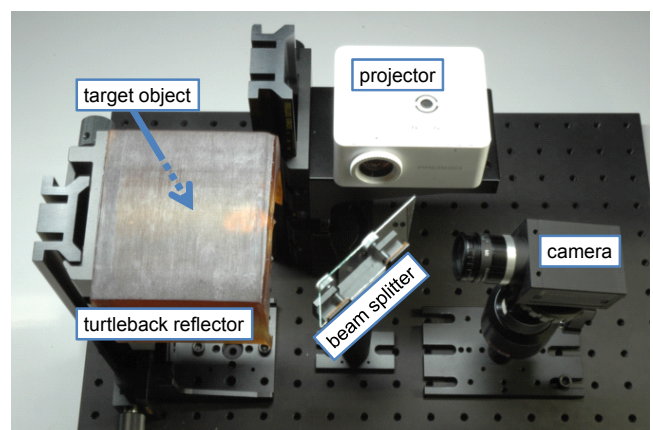


Fig. 8 Total optical device for hemispherical confocal imaging.

tal facets, which are located at the border of the upper and lower hemispheres. In total we used 91 facets.

In the design shown in Fig. 2 (b), the target object occludes some mirrors. Hence, we combined two ellipsoids as shown in Fig. 5. In this design, the two polyhedral mirrors place the virtual cameras over the whole surface of the hemisphere.

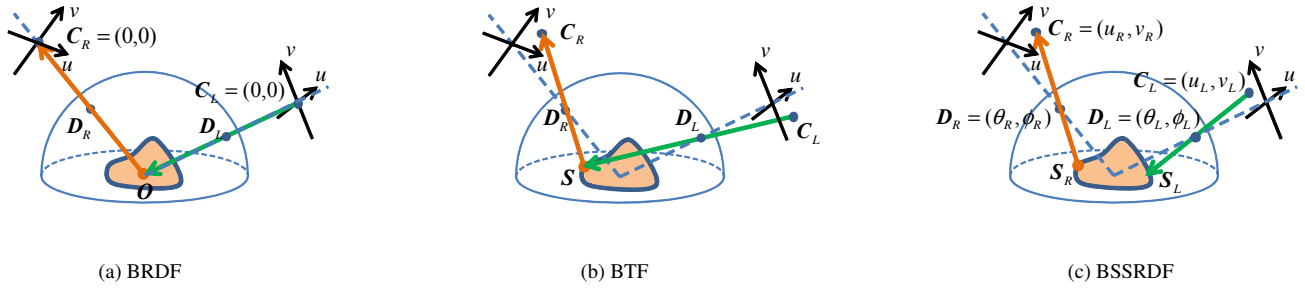


Fig. 9 Reflectance properties represented with 8DRF.

We designed one polyhedral mirror because pairs of polyhedral mirrors are symmetrical. To fix the mirror patches, we designed a frame as shown in Fig. 6. This frame is made by stereolithography and planar mirror patches are attached to the frame. Fifty mirror patches completely cover half of the hemisphere. The frame with mirror patches is the *turtleback reflector* as shown in Fig. 7.

Here, we combine the turtleback reflector with a coaxial pairing of a high-resolution camera (PointGrey, Grass-50S5C, 2448×2048) and a small projector (KAIREN Projector X Pro920, 640×480) using a beam splitter as shown in Fig. 8.

The device is designed to measure a small area of 6×6 mm. By resampling the captured image using a real camera, images of the virtual cameras whose resolution is 60×60 pixels are generated. For a virtual projector, we resample the target area using a 20×20 format. Hence, the resolution of the virtual projector corresponds to 20×20 pixels.

4. Slices of 8-D Reflectance Field

4.1 Overview of Low-Dimensional Slices

8DRFs have much information on a scene. So, appropriate slices represent useful functions (Fig. 9, Table 1). To represent reflectance properties, all the dimensions are not always needed. Here, I describe three reflectance properties as slices of an 8DRF. First, I show a slice that can represent reflectance of an opaque material. Next, I show a slice that can represent reflectance of a texture. Finally, I show a slice that can represent reflectance of a translucent object.

4.2 Bidirectional Reflectance Distribution Function

For opaque objects with uniform reflectance property, the property of only one point on the surface can represent the reflectance properties for all points of whole surface. It is the Bidirectional Reflectance Distribution Function (denoted as BRDF in the following).

In the BRDF, the observed point is only one. So, it can be the center (0, 0) of the hemisphere. When the target point is illuminated in the direction D_L , the reflected light in the direction D_R can be represented in BRDF as

$$BRDF(D_L, D_R) = F(D_L, (0, 0), D_R, (0, 0)). \quad (2)$$

Thus, we can see that the BRDF is the four-dimensional slice of the 8DRF as shown in Fig. 9 (a).

Table 1 Low dimensional slices and Applications.

	Representations with 8DRF
$BRDF(D_L, D_R)$	$F(D_L, (0, 0), D_R, (0, 0))$
$BTF(D_L, S, D_R)$	$F(D_L, P_L(D_L, S), D_R, P_R(D_R, S))$
$BSSRDF(D_L, S_L, D_R, S_R)$	$F(D_L, P_L(D_L, S_L), D_R, P_R(D_R, S_R))$

4.3 Bidirectional Texture Function

For opaque objects with partially varying reflectance properties, on the surface, the points to be measured are all the surface points of the objects. It is the Bidirectional Texture Function (denoted as BTF in the following).

The difference between the BTF and BRDF is the number of target points. In the BTF, the target points are not the only one. For the point at $S = (x, y, z)$ on the object surface, when only the point S is illuminated, the reflected light is measured only in the directions passing S . Thus, denoting the illumination and reflection direction as projective transformations, $P_L(D_L, S)$ and $P_R(D_R, S)$, respectively, the intensity of reflected light in the BTF is represented as

$$BTF(D_L, S, D_R) = F(D_L, P_L(D_L, S), D_R, P_R(D_R, S)). \quad (3)$$

In this way, we can see that the BTF is the six-dimensional slice of an 8DRF as shown in Fig. 9 (b).

4.4 Bidirectional Scattering Surface Distribution Function

For translucent objects, the incident light on the surface spreads to the inside of the objects and the reflected light observed not only the incident point but other points. This inside scattering is called as the subsurface scattering, and represented by Bidirectional Scattering Surface Reflectance Distribution Function (denoted as BSSRDF in the following).

In this section, the illuminated and observed points are denoted as $S_L = (x_L, y_L, z_L)$ and $S_R = (x_R, y_R, z_R)$, respectively. The direction of rays passing through a point D_L on the hemisphere and illuminating the point S_L can be represented by $C_L = P_L(D_L, S_L)$ using a projective transformation P_L . Thus, the intensity in the BSSRDF can be represented using the incident direction D_L , incident point S_L , observed point S_R , and outgoing direction D_R as

$$BSSRDF(D_L, S_L, D_R, S_R) = F(D_L, P_L(D_L, S_L), D_R, P_R(D_R, S_R)). \quad (4)$$

So, the BSSRDF is another representation of the 8DRF as shown in Fig. 9 (c).

5. Framework of 8-D Reflectance Field for Computational Photography

We often want to change the focusing or illumination conditions of photographs after they are captured, hence, some computational photography techniques have been proposed. For refocusing, the synthetic aperture [39] can tighten the depth-of-field or shift the focal plane. For relighting, the Light Stage [6] can generate images of the target object under arbitrary illumination conditions. Moreover, by controlling both focus and illumination, the confocal imaging [23] can clearly visualize a particular depth.

The formulation and the implementation of these computational photography techniques are optimized to a specific situation because they are specialized for different purposes in different research fields. Hence, the relationship between them has been unclear.

In this section, we introduce a unified framework to explain computational photography techniques based on an 8-D reflectance field (8DRF). The 8DRF represents the relationship between 4-D illumination and 4-D observation light fields. Since the 8DRF includes all information about illumination and reflection, the synthetic aperture, the image-based relighting, and the confocal imaging techniques can be explained as a computation of the 8DRF in the proposed framework. To confirm the validity of our framework, we have implemented these computational photography techniques on one system using the Turtleback Reflector [35], which is only one device for sampling an 8DRF over a hemisphere at uniform intervals.

5.1 Framework to Compute 8-D Reflectance Field

To formulate the computation of an 8DRF, I derive the framework to image the 8DRF. An image represents the appearance of the captured scene in two-dimensional data. So, the destination of the computation is to acquire a pixel value $I(\mathbf{D}, \mathbf{C})$ for the given direction (\mathbf{D}, \mathbf{C}) . In the lens optics, the pixel intensity is given by integration of ray intensities passing through the lens. Thus, to acquire a pixel value, many rays in various directions are associated to the given direction (\mathbf{D}, \mathbf{C}) and the intensities are integrated. The integrated intensities are provided by a 4DLF of reflection from the scene. However, an 8DRF cannot directly represent a reflection light field because it gives us reflectance of the scene. So, at first, I compute the reflection light field by an 8DRF.

The reflection light field is the reflected light from the scene under an illumination condition. So, to compute the reflection 4DLF, an 8DRF $F(\mathbf{D}_L, \mathbf{C}_L, \mathbf{D}_R, \mathbf{C}_R)$ and an illumination light field $L(\mathbf{D}_L, \mathbf{C}_L)$ are needed. The reflection light field $R(\mathbf{D}_R, \mathbf{C}_R)$ can be derived as

$$R(\mathbf{D}_R, \mathbf{C}_R) = \iint F(\mathbf{D}_L, \mathbf{C}_L, \mathbf{D}_R, \mathbf{C}_R) \cdot L(\mathbf{D}_L, \mathbf{C}_L) d\mathbf{D}_L d\mathbf{C}_L. \quad (5)$$

As mentioned before, a lens focuses light rays from the scene at a point on an imaging plane. Here, the observed point also reflects many rays in the other directions as well as the captured rays. It is a selection of rays from the scene. So, I compute the selected rays $R'(\mathbf{D}_R, \mathbf{C}_R)$ to be integrated, as the masked reflection light field by a mask function $M(\mathbf{D}_R, \mathbf{C}_R)$ as

$$R'(\mathbf{D}_R, \mathbf{C}_R) = R(\mathbf{D}_R, \mathbf{C}_R) \cdot M(\mathbf{D}_R, \mathbf{C}_R). \quad (6)$$

Therefore, the target pixel intensity is computed as

$$I(\mathbf{D}, \mathbf{C}) = \iint R'(\mathbf{D}_R, \mathbf{C}_R) d\mathbf{D}_R d\mathbf{C}_R. \quad (7)$$

Totally, in the framework to compute an image from an 8DRF, I can get an image by a measured 8DRF of the scene $F(\mathbf{D}_L, \mathbf{C}_L, \mathbf{D}_R, \mathbf{C}_R)$, a given arbitrary illumination condition $L(\mathbf{D}_L, \mathbf{C}_L)$, and an optical ray selection $M(\mathbf{D}_R, \mathbf{C}_R)$ as

$$I(\mathbf{D}, \mathbf{C}) = \iiint F(\mathbf{D}_L, \mathbf{C}_L, \mathbf{D}_R, \mathbf{C}_R) \cdot L(\mathbf{D}_L, \mathbf{C}_L) \cdot M(\mathbf{D}_R, \mathbf{C}_R) d\mathbf{D}_L d\mathbf{C}_L d\mathbf{D}_R d\mathbf{C}_R. \quad (8)$$

5.2 Implementations of Elemental Computational Photography

In this section, we formulate some computational photography techniques for the computation of an 8DRF in a unified framework. We unify the synthetic aperture, image-based relighting, and confocal imaging.

The synthetic aperture technique [39] realizes a virtual shallow depth-of-field (DoF). The imaging technique accumulates aligned multi-viewpoint images captured by a shifting camera or a camera array. Since the focal depth can be adaptively shifted by changing the aligned position, it is useful for refocusing.

The synthetic aperture can be formulated as a computation of an 8DRF. We synthesize an aperture A centered at \mathbf{D}_R as shown in **Fig. 10**. The focal plane is defined as a surface Π . The focused point S is derived by the intersection of the focal plane Π and a viewing ray passing through \mathbf{D}_R along \mathbf{C}_R . The mask function M , whether or not a ray passes through the point S and the aperture A :

$$M(\mathbf{D}, \mathbf{C}, S, A) = \begin{cases} 1: & \text{if the ray passes } S \text{ and } \mathbf{D} \in A \\ 0: & \text{otherwise.} \end{cases} \quad (9)$$

The synthetic aperture imaging can be represented by integration of the eight dimensional reflectance field F with the mask function over the hemisphere. The following expression derives the intensity I of a pixel \mathbf{C}_R on the image captured by a virtual camera with the aperture A and viewpoint \mathbf{D}_R :

$$I(\mathbf{D}_R, \mathbf{C}_R, A, \Pi) = \iiint F(\mathbf{D}_L, \mathbf{C}_L, \mathbf{D}'_R, \mathbf{C}'_R) \cdot F_L(\mathbf{D}_L, \mathbf{C}_L) \cdot M(\mathbf{D}'_R, \mathbf{C}'_R, S, A) \cdot d\mathbf{D}_L d\mathbf{C}_L d\mathbf{D}'_R d\mathbf{C}'_R, \quad (10)$$

where S is a function of $\mathbf{D}_R, \mathbf{C}_R$ and Π . F_L is given as a constant 4DLF of illumination. The turtleback reflector can produce an extremely large aperture using the synthetic aperture technique. To evaluate the DOF, a textured paper is captured using a hemispherical synthetic aperture. We synthesize an aperture focused on a plane with 0.1mm increments between $z = 0.0\text{mm}$ and $z = 0.5\text{mm}$. As shown in **Fig. 11**, the image at $z = 0.2\text{mm}$ is the most focused and the images at $z = 0.0\text{mm}$ and $z = 0.4\text{mm}$ are blurred explicitly. Therefore, the DOF provided by the turtleback reflector is about 0.4mm. This DOF is not very shallow because we implemented only half of the turtleback reflector. However, we confirmed the ability to make a shallow DOF.

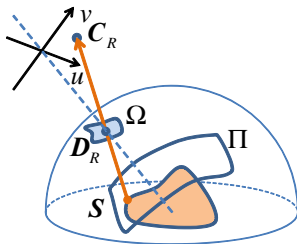


Fig. 10 Synthetic aperture. This is achieved by an accumulation of intensities of rays passing through an aperture to make a target focal plane.

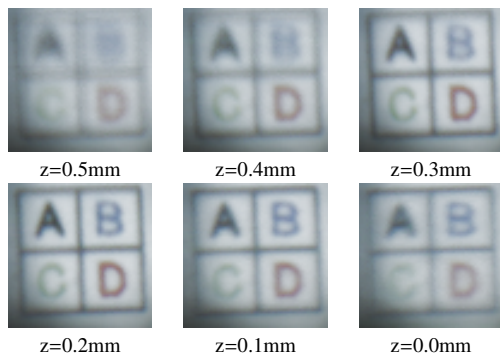


Fig. 11 Sweeping focal plane.

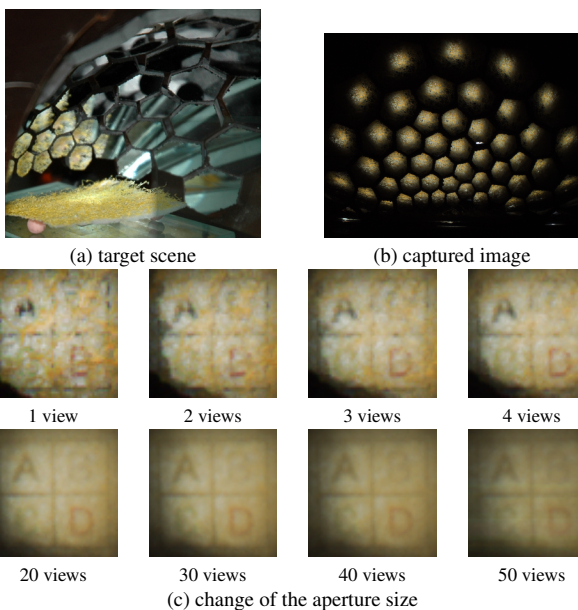


Fig. 12 Results for synthetic aperture using our optical device.

Next, a textured paper was covered using an obstacle of yellow dense mesh, as shown in **Fig. 12** (a). A white uniform pattern was projected onto the scene. Figure 12 (b) shows the captured image from the real camera. This image includes 50 views corresponding to 50 virtual cameras. Because all the views are affected by the obstacle, it is difficult to see the texture of the paper. Figure 12 (c) shows the change in appearance when the number of virtual cameras increases to synthesize a large aperture. Because our optical device can synthesize half the hemispherical aperture, the obstacle is completely blurred and the texture becomes clear with an increasing number of virtual cameras.

Figure 13 shows the result of the synthetic aperture on our framework using our 8DRF measuring device. This imaging technique synthesizes the shallow DoF images. The experimen-

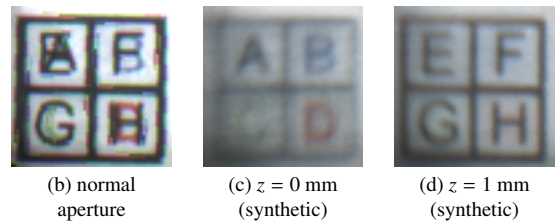
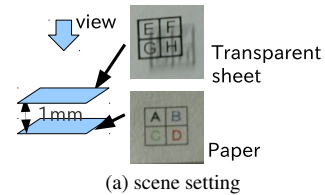


Fig. 13 The results of the synthetic aperture. The scene consists of a textured film and textured paper 2 mm beneath it. In the normal aperture image, both the textures are mixed. In the synthetic images, the textures are separately focused and can be read.

tal scene consists of the textured film over the textured paper as shown in (a). Since the gap between the two layers is only 1 mm, the two textures are mixed if a normal camera is used as shown in (b). The images (c) and (d) are the results of refocusing on the film and the paper. We can see that two layers are well separated. This confirms the synthetic aperture is successfully accomplished using the 8DRF measuring device.

The image-based relighting technique can generate a realistic image of a scene under arbitrary illumination [6]. The technique is achieved using a simple combination of the captured images under different illuminations.

This technique is also formulated on an 8DRF. Illumination of the scene is completely described by a four dimensional illumination light field F_L . For a camera fixed at D_R , as shown in **Fig. 14**, the intensity I of the pixel C_R of the camera image can be expressed as:

$$I(D_R, C_R, F_L) = \iint F(D_L, C_L, D_R, C_R) \cdot F_L(D_L, C_L) dD_L dC_L. \quad (11)$$

The F_L can be given arbitrarily.

Figure 15 shows the results of the image-based relighting on our framework using the 8DRF measuring device. The target object is a metallic ring (a) which has complex reflectance properties. In general, it is difficult to synthesize a realistic view under arbitrary illumination by modeling the reflectance. The top row of (b) shows the illumination conditions*¹. Fifty pixel values were sampled for illumination because the used device has fifty light sources. The bottom row shows the synthesized images corresponding to the illumination conditions approximately generated by fifty point light sources.

The confocal imaging technique is used in microscopy. It can clearly create an image at the depth of interest by simultaneously scanning the illumination and observation using a pinhole.

The confocal imaging can be formulated as a computation of an 8DRF because an 8DRF can synthesize a large aperture for both illumination and observation. Scanning a pinhole synthesizes a virtual aperture A at the center point D on a hemispherical

*¹ The images are Debevec's light probe images at <http://ict.debevec.org/~debevec/Probes/>

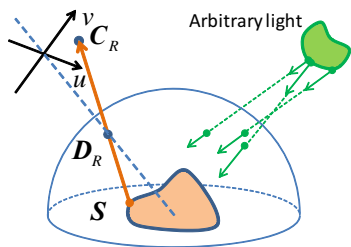


Fig. 14 Image-based relighting. Given the illumination condition, the images can be synthesized from the corresponding observations in the 8DRF.

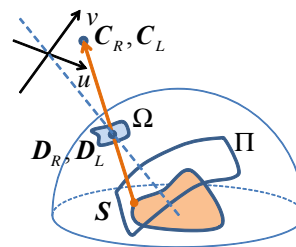


Fig. 16 Confocal imaging. The observation and illumination have the same focal plane.

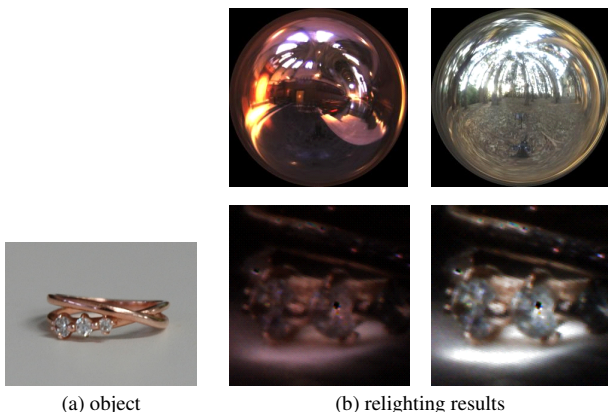


Fig. 15 The results of the image-based relighting. For the given illuminations (top row), the corresponding appearances can be reproduced by simple computation of the 8DRF (bottom row).

surface. The target focal surface in the scene is given as Π .

The mask function M indicates whether the ray from a focused point S on the focal plane Π passes through the aperture A as shown in **Fig. 16**.

$$M(\mathbf{D}, \mathbf{C}, S, A) = \begin{cases} 1: & \text{if the ray passes } S \text{ and } \mathbf{D} \in A \\ 0: & \text{otherwise} \end{cases} \quad (12)$$

The confocal imaging can be represented by integration of the 8DRF with the mask function. The following expression derives the intensity I of a pixel C_R on the image captured by a virtual aperture A for both illumination and observation and the view-point D_R :

$$I(\mathbf{D}_R, \mathbf{C}_R, A, \Pi) = \iiint \iiint F(\mathbf{D}_L, \mathbf{C}_L, \mathbf{D}'_R, \mathbf{C}'_R) \cdot M(\mathbf{D}_L, \mathbf{C}_L, S, A) \cdot M(\mathbf{D}'_R, \mathbf{C}'_R, S, A) \cdot d\mathbf{D}_L d\mathbf{C}_L \cdot d\mathbf{D}'_R d\mathbf{C}'_R \quad (13)$$

Figure 17 shows the result of the confocal imaging on our framework using the 8DRF measuring device. The target scene consists of the target textured paper beneath an occluding orange mesh as shown in (a). In a view captured by a normal camera, the orange mesh occludes the texture as in (b). Although, as shown in (c), the synthetic aperture can blur the mesh, the texture is still unclear. The result of confocal imaging presents clear texture of the paper and less effect from the mesh as shown in (d).

6. Analytical Imaging Technique using 8-D Reflectance Field

The previous section describe the techniques using conven-

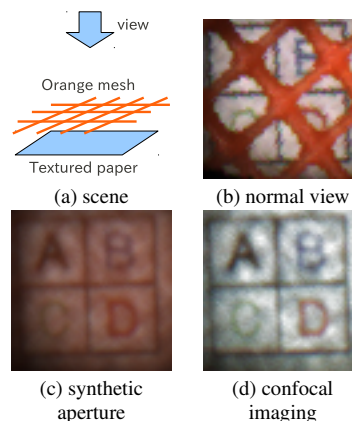


Fig. 17 The result of confocal imaging. The scene consists of the textured paper and overlapped orange mesh. In the normal view, the textured paper is partially occluded by the mesh. In the synthetic aperture image, the texture is recognizable because the mesh is significantly blurred, while the orange color remains. In the confocal image, the texture becomes clear because the mesh is significantly blurred and less illuminated.

tional optics and its implementation results using our framework that makes an image by simple integration of a reflectance field. Although the framework shows flexibility of a reflectance field, it did not add novelty. In this section we show a novel imaging technique that analyze an 8-D reflectance field to clearly visualize a particular depth of occluded or scattering scenes.

Let us assume that a 3-D scene is illuminated by a light source and observed by a camera as shown in **Fig. 18**. Even if the camera is focused on a particular depth in the scene, the captured image includes reflections from the entire scene. To observe the particular depth, only that depth should be illuminated. This means that both the illumination and the observation should have a shallow DOF.

Even if we succeed in illuminating only the particular depth, clear views cannot be observed. The major reasons for this are *scattering* and *attenuation*. The scattering is caused by multi-bounce reflections in the translucent media, which cause the views to become blurred. The attenuation is caused by *occlusion* due to obstacles or *absorption* due to low transparency media. Under this attenuation, the illumination becomes nonuniform and the reflections are partially darkened. The following four functions are required to obtain clear views of a particular depth in a 3-D scene.

- (a) The DOF should be as shallow as possible.
- (b) Only the particular depth of interest should be illuminated.
- (c) Scattering should be eliminated.

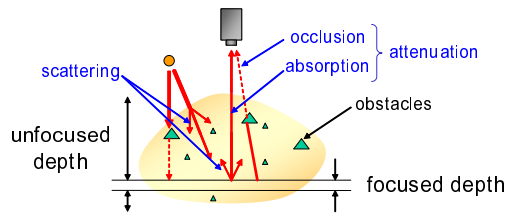


Fig. 18 Illumination and reflection in a 3-D scene. It is difficult to observe a particular depth due to scattering and attenuation.

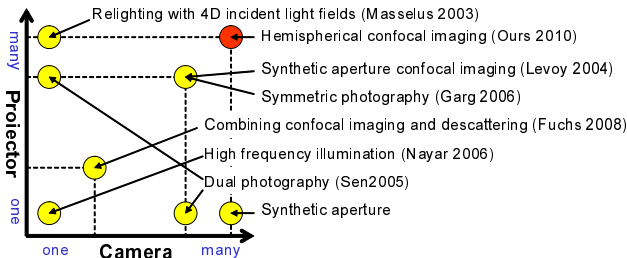


Fig. 19 The numbers of projectors and cameras of several imaging methods which use projector(s) and camera(s) for reflection analysis or reflectance field measurement.

(d) Attenuation should be eliminated.

To satisfy these requirements, we propose *hemispherical confocal imaging* consisting of (1) a specially designed *turtleback reflector*, (2) *focused high frequency illumination*, and (3) *factorization* of observed views.

The turtleback reflector with coaxial camera and projector synthesizes a hemispherical aperture for both illumination and observation to satisfy (a). The focused high frequency illumination eliminates reflections from the unfocused depth and global reflection to solve (b) and (c). We then factorized the observed views into masking, attenuation, reflected light, illuminance, and texture terms to solve for (d). The advantages and disadvantages and the numbers of projectors and cameras for several imaging methods are summarized in **Table 2** and **Fig. 19**. Although we explained that unfocused depths are ‘unilluminated’ by the synthetic aperture confocal imaging and our hemispherical confocal imaging, the depths are actually illuminated, but these illuminations are eliminated by subtractive calculation. Hence, image noise may increase.

6.1 Focused high frequency illumination

To analyze the reflectance field in a 3-D scene, we need to know how light illuminates points in a scene, and how the reflections are observed. We divide the 3-D scene into a set of small voxels. Let L be an illumination on the scene, and $R_k(L)$ be an image component that consists of a set of reflected and scattered lights from the k -th voxel under the illumination L as shown in **Fig. 20** (a). Because the observed image of the entire scene by a camera is expressed as a sum of the reflected and scattered lights from all voxels, the image is represented by $\sum_i R_i(L)$.

Illuminations and reflections can be regarded as the sum of the direct and global components [28]. As shown in **Fig. 20** (b), the illumination can be decomposed into direct L^D and global illuminations L^G as

$$L = L^D + L^G. \quad (14)$$

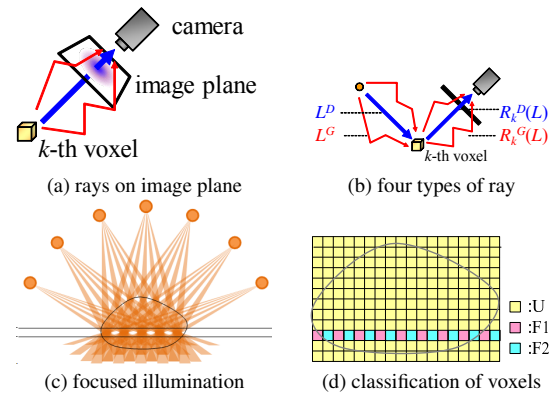


Fig. 20 Focused high frequency illumination. The high frequency patterns are focused only on the particular depth. The projection is blurred out of the DOF.

Similarly, the reflection can also be decomposed into the direct $R_k^D(L)$ and global reflections $R_k^G(L)$. The R_k^D is recorded as the pixel intensity at the intersection of the image plane and the line between the k -th voxel and the camera, while the R_k^G is recorded as the part of the intensity of other pixels as shown in **Fig. 20** (a).

The image component $R_k(L)$ can be decomposed into the direct and global components as

$$R_k(L) = R_k^D(L) + R_k^G(L). \quad (15)$$

It is easy to assume that the R_k is a linear function by disabling the gamma correction of the camera. Hence, the observed image can be modeled as the sum of four components by

$$\begin{aligned} \sum_i R_i(L) &= \sum_i R_i^D(L^D) + \sum_i R_i^D(L^G) \\ &+ \sum_i R_i^G(L^D) + \sum_i R_i^G(L^G). \end{aligned} \quad (16)$$

To obtain clear views of a particular depth in a 3-D scene, only that depth should be illuminated. Any global illuminations and global reflections should be eliminated to reduce scattering in the media. That is, direct reflections by direct illuminations, $R_k^D(L^D)$, from the particular depth should be measured separately.

Fuchs et al. [8] proposed the descattered confocal imaging technique to capture a clear view of a particular depth in scattering media. They combined the focused illumination technique proposed by Levoy et al. [18] and the high frequency illumination technique proposed by Nayar et al. [28]. They captured clear descattered images by line scanning confocal imaging. However, this technique could not deal with reflections from opaque objects in the unfocused depth. The reflections were introduced as the floodlit contribution by Levoy et al. [18]. They removed them using many observations under a lot of random pattern illuminations.

Here, we propose a new imaging method, called *focused high frequency illumination (FHFI)*, based on descattered confocal imaging [8]. Our technique can remove the floodlit contribution and requires only constant measurement time. The FHFI uses a lot of projectors placed over a wide range on a hemisphere.

For the FHFI, high frequency checkerboard patterns are projected from each projector. The positions of the white and black pixels are aligned at the depth as shown in **Fig. 20** (c). This means

Table 2 Comparison of several imaging methods.

	unfocused depth	scanning	scattering
Synthetic aperture	bright	unnecessary	remaining
Confocal imaging	darken	necessary	remaining
Synthetic aperture confocal imaging [18]	unilluminated	unnecessary	remaining
Confocal imaging with descattering [8]	darken	necessary	reduced
Our hemispherical confocal imaging	unilluminated	unnecessary	reduced

that the high frequency illumination is focused only at a particular depth. The voxels in the scene are classified into unfocused voxels U , focused and illuminated voxels $F1$, and focused but unilluminated voxels $F2$ as shown in Fig. 20 (d).

It is noted that synthetic aperture illumination with regular patterns like checkerboards often cause artifacts of periodic patterns at depths other than the focal plane [42]. This artifact occurs when the projected patterns are accidentally aligned at different depths. This problem can be reduced by the hemispherical placement of the virtual projectors because projected patterns do not align at different depths.

When compared with a white pattern, the average intensity of the high frequency illumination is darker because half the pixels are black. **Table 3** shows the relative intensities of the four reflection components for each voxel type. The global illumination to each voxel decreases by half. The direct illumination to U voxels also decreases by half because the projected patterns are blurred. Therefore, the floodlit contribution decreases by half under the FHFI using the turtleback reflector. The $F1$ voxels receive full direct illumination, while the $F2$ voxels receive no direct illumination. By combining these differences, $\sum_{i \in F1 \cup F2} R_i^D(L^D)$ which enables only direct components from voxels at the focused depth to be separated.

Let I_P be a captured image when voxels of $F1$ are illuminated but voxels of $F2$ are not illuminated. Let I_N be a captured image when the inverse pattern is projected. Then, these images can be expressed as

$$I_P = \sum_{i \in F1} R_i \left(L^D + \frac{L^G}{2} \right) + \sum_{i \in F2} R_i \left(\frac{L^G}{2} \right) + \sum_{i \in U} R_i \left(\frac{L^D + L^G}{2} \right), \quad (17)$$

$$I_N = \sum_{i \in F1} R_i \left(\frac{L^G}{2} \right) + \sum_{i \in F2} R_i \left(L^D + \frac{L^G}{2} \right) + \sum_{i \in U} R_i \left(\frac{L^D + L^G}{2} \right). \quad (18)$$

The absolute difference of two intensities in I_P and I_N is then calculated for each pixel. Since this is a pixel-wise process, the pixel intensities at coordinates (x, y) in I_P , I_N , and $R(L)$ are expressed as $I_P(x, y)$, $I_N(x, y)$, and $R(L, x, y)$. The absolute difference I_D is calculated by

$$\begin{aligned} I_D(x, y) &= |I_P(x, y) - I_N(x, y)| \\ &= \left| \sum_{i \in F1} R_i(L^D, x, y) - \sum_{i \in F2} R_i(L^D, x, y) \right| \\ &= \left| \sum_{i \in F1} R_i^D(L^D, x, y) + \sum_{i \in F1} R_i^G(L^D, x, y) \right| \end{aligned}$$

$$- \sum_{i \in F2} R_i^D(L^D, x, y) - \sum_{i \in F2} R_i^G(L^D, x, y) \Big|. \quad (19)$$

If we can assume a locally homogeneous surface, the global component does not change even if the phase of the high frequency pattern shifts [8], [28]. Therefore,

$$\sum_{i \in F1} R_i^G(L^D, x, y) \approx \sum_{i \in F2} R_i^G(L^D, x, y). \quad (20)$$

Moreover, $\sum_{i \in F1} R_i^D(L^D, x, y)$ and $\sum_{i \in F2} R_i^D(L^D, x, y)$ are exclusive. That is, when the voxels of $F1$ are illuminated, the former becomes large while the latter becomes zero and vice versa. Hence,

$$\begin{aligned} I_D(x, y) &= \left| \sum_{i \in F1} R_i^D(L^D, x, y) - \sum_{i \in F2} R_i^D(L^D, x, y) \right| \\ &= \sum_{i \in F1} R_i^D(L^D, x, y) + \sum_{i \in F2} R_i^D(L^D, x, y) \\ &= \sum_{i \in F1 \cup F2} R_i^D(L^D, x, y). \end{aligned} \quad (21)$$

This means that only the particular depth ($F1 \cup F2$) can be directly illuminated without global illuminations, and only the direct reflections can be measured without global reflections. As shown in Table 3, our method does not illuminate the unfocused depth. Because no scanning is necessary, the measurement is fast. Furthermore, scattering, which is a major global component in translucent media, is eliminated.

6.2 Factorization of the observed views

By the FHFI introduced in the previous section, only the focused depth is illuminated and global components such as scattering are eliminated. However, the obtained view may still be unclear because illumination and reflected light attenuate. The reason for the attenuation is the *occlusion* and *absorption* as shown in Fig. 18.

These are similar but different optical phenomena. Occlusion directly interrupts reflected light by opaque obstacles. Hence, it causes very dark regions with sharp edges in the observed image. On the other hand, absorption decreases lighting powers by low transparency media. It causes smooth unevenness in the observed image. To obtain a clear view at a particular depth of the scene, the optical effects of occlusion and absorption should be eliminated.

The attenuation occurs in both observation and illumination. However, if the observation and illumination are coaxial, the attenuation effects are the same. Hence, we can estimate the attenuation of the observation.

When a region in a captured image is dark, we cannot directly know why the reflectance is low or the illumination is weak. It is difficult to eliminate attenuation effects using only a single image. Fortunately, the scene is observed from many virtual cameras. Even if some lights are not observed from a camera, other

Table 3 Relative intensities of four reflection components for each voxel type.

	$R_k^D(L^D)$	$R_k^D(L^G)$	$R_k^G(L^D)$	$R_k^G(L^G)$
U (unfocused)	1/2	1/2	1/2	1/2
F1 (focused and illuminated)	1	1/2	1	1/2
F2 (focused and unilluminated)	0	1/2	0	1/2

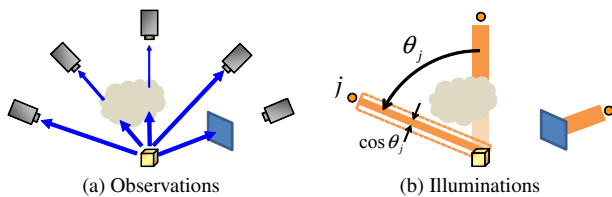


Fig. 21 Attenuation effects.

cameras may observe the scene without attenuation as shown in **Fig. 21** (a). Hence, we try to estimate texture that is not affected by attenuation based on observation from multiple cameras.

To factorize the observed intensities into reflected light and the attenuation, we assume that surface reflections can be expressed by the Lambert model. That is, the observed brightness is independent of the viewing angle. We assume that there are K virtual cameras and each camera has N pixels. Let O_{ij} be the intensity of the i -th pixel in the j -th camera. In our model, the observed intensities are factorized as

$$O_{ij} = M_{ij}A_{ij}R_i. \quad (22)$$

Here, M_{ij} is the *masking term* which has a value of 0 or 1. If the light is occluded by obstacles, the value becomes 0 otherwise it becomes 1. A_{ij} is the *attenuation term*, which expresses light attenuation due to absorption. R_i is the *reflected light term* which expresses reflected light of the particular depth under attenuated illumination. It is noted that only the reflected light term is independent of the viewing direction, assuming Lambertian reflection. Figure 22 illustrates this relationship.

The flow of the factorization process is as follows

STEP-1: First, the masking term is decided. Since unfocused depths are not illuminated by the FHFI, obstacles can easily be distinguished using a simple threshold. After making the decision on the masking term, the following processes are conducted for pixels satisfying $M_{ij} = 1$.

STEP-2: The initial attenuation term is decided as $A_{ij} = 1$.

STEP-3: The reflected light term is calculated. Ideally, a unique reflected light should be estimated despite the different camera j , but the observed intensities vary. This kind of problem is often seen in stereoscopy [38], so we used a median filter in a similar fashion by $R_i = \text{Median}(O_{ij}/A_{ij})$.

STEP-4: The attenuation term is updated by $A_{ij} = O_{ij}/R_i$ to satisfy Eq.(22).

STEP-5: The attenuation term is smoothed using a Gaussian function, because the attenuation varies smoothly over the 3-D scene. After this, return to **STEP-3** and repeat until the texture term does not change.

Using this factorization process, the observed views are decom-

posed to three terms and we can obtain the reflected light of the particular depth without attenuation of the observation.

Although the reflected light term R_i is estimated, it includes the attenuation effects of the illumination. Hence, we estimate the texture term T_i , which is independent of the illumination, by eliminating attenuation effects in the reflected light term. First, a maximum illuminance on the surface is estimated. The maximum illuminance is the illuminance when there are no obstacles. The illuminance from the j -th virtual projector weakens in proportion to $\cos \theta_j$, where θ_j is the zenith angle as shown in Fig.10(b). Here, we can assume that the illuminance is uniform over the surface by assuming that the observation area is small. Hence, the maximum illuminance L_i^m for i -th pixel can be expressed by the sum of illuminance from all virtual projectors as follows,

$$L_i^m = \sum_j \cos \theta_j. \quad (23)$$

Since the j -th virtual projector and the j -th virtual camera are placed at the same position, we can regard the attenuation term A_{ij} as the attenuations of the illumination from the j -th virtual projector on the i -th pixel. Hence, the sum of the attenuated illuminance L_i^a is expressed as

$$L_i^a = \sum_j M_{ij}A_{ij} \cos \theta_j. \quad (24)$$

Therefore, the texture term T_i is restored by

$$T_i = R_i L_i^m / L_i^a. \quad (25)$$

Through these processes, the observed views are decomposed into a masking term, attenuation term, illuminance, and texture term. In this texture term, both the attenuation effects of the observation and the illumination are eliminated.

Stability of the masking term

Pixel-wise masking is often used for merging multiple images. Wilburn et al. [42] used a mask to reconstruct an alias-free synthetic aperture image. They decided on a mask based on the variance of corresponding pixels.

On the other hand, we used a simple threshold. In general, shadow regions are not perfectly black because of global illumination. However, our FHFI can effectively eliminate the global components in advance. Hence, pixel intensities in shadow regions become close to zero, and the regions can be segmented stably.

Our factorization process strongly depends on the Lambert model. We assume that intensities observed by multiple cameras become constant if there is no attenuation. Hence, if the diffuse assumption is violated and strong specular reflections are observed, the factorization does not work well.

6.3 Experiments of Hemispherical Confocal Imaging

First, we confirmed that the FHFI is effective for descattering

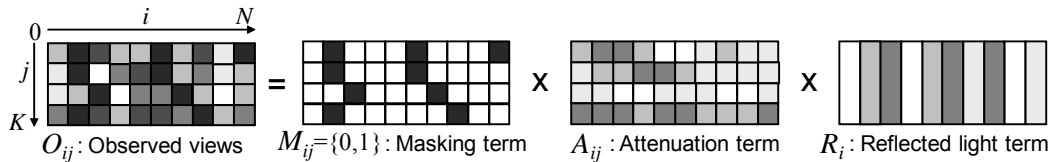


Fig. 22 Concept of factorization. The observed intensities are factorized into masking, attenuation, and reflected light terms to reduce attenuation.

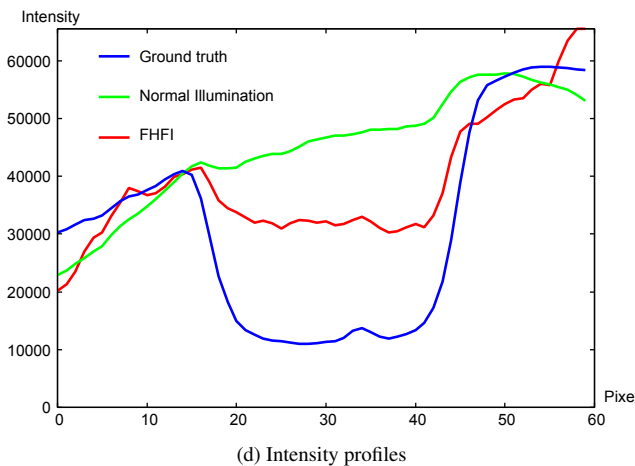
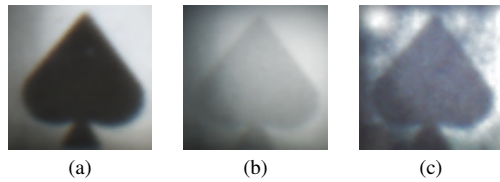


Fig. 23 Descattering by focused high frequency illumination.

in a 3-D volume. The textured paper in Fig. 23 (a) is covered by a sponge as in (b). Since the sponge scatters lights strongly, edges are blurred.

In theory, only two illumination patterns are needed for the FHFI. However, the illuminated pattern becomes blurred at the edges. Hence, we used checkered patterns, in which white and black are replaced every three pixels and shifted the pattern by one pixel. In total, 18 illumination patterns are projected from the virtual projectors so that these patterns are aligned on the paper. As Nayar et al. [28] did, we took maximum and minimum intensities for each pixel position in the 18 images. Then, the difference image can be obtained.

Figure 23 (c) shows the direct component obtained by the FHFI. We can see that scattering in the 3-D scene is reduced and the contrast is improved. To show how much the contrast was improved, we analyzed the intensity profiles of the images as shown in Fig. 23 (d). This graph shows intensity profiles along a horizontal line at the mid height of the images. The central region from 20 to 40 corresponds to the black part of the spade figure. We can see that the contrast was improved by descattering. The descattering effect is not perfect, which is attributed to the low resolution of the virtual projectors in the current prototype system.

We confirmed the ability to visualize a particular depth in a 3-D scene by combining the FHFI and the factorization. The factorization reduces attenuation effects of occlusion and absorption.

Hence, we evaluated them separately.

In the first experiment, we used a scene with occluders. Figure 24 (a) shows the scene where an orange mesh covers a textured paper, and (b) shows all views from the virtual cameras under normal illumination^{*2}. By simply averaging these views, a synthetic aperture image can be generated, as shown in (c). Although the obstacle is blurred, the orange color of the mesh affects the paper. Confocal imaging [23] can generate a better image as shown in (e) because the orange mesh is less illuminated.

The mesh becomes dark under the FHFI because it is not illuminated, while the paper is bright, as shown in (h). By averaging these views, the dark mesh is blurred and the orange color correctly disappears, as shown in (d). However, there are uneven dark regions due to attenuation. The factorization decomposes the observed views (h) into the masking term (i), the attenuation term (j), and the reflected light term (f). We then estimate the illuminance (k) and the texture term (l) using these decomposed terms. We see that the attenuation is reduced, especially around the letters of the black 'A' and the red 'D', since the occlusion due to the mesh is regarded as masking. On the other hand, comparing (l) with (f), the attenuation is too reduced under the letter 'B' because of the inaccurate masking term. Around the edges of obstacles, the masking term cannot be accurately estimated due to the low resolution of the virtual cameras.

While the difference compared with the ground truth image (g) that was captured without the orange mesh is not small, we confirmed that the image without the DOF can be made to almost disappear by hemispherical confocal imaging.

In the second experiment, we used a scene with an inhomogeneous translucent absorber. A target scene consists of a textured paper of Fig. 25 (a) with cotton waste on the paper. A normal view (d) is unevenly attenuated. In the direct components obtained by the FHFI, attenuation still remains as in (b). Figure 25 (e) shows the attenuation term, and expresses smooth change of absorption and (f) shows the texture term.

While the attenuation and texture terms were factorized, the effectiveness was weak. Figure 25 (c) shows a simple average of (d). The difference between (c) and (f) is small. One of the possible reasons is calibration errors. In fact, the hemispherical synthetic aperture and the FHFI effectively improved the appearance. However, accurate geometric calibration of virtual cameras is required for the factorization. Another reason is that the FHFI did not completely remove scatterings due to the low resolution, while the factorization assumes that images have no scattering.

*2 Although there are 50 mirror patches, only 48 patches were used because two patches were misaligned.

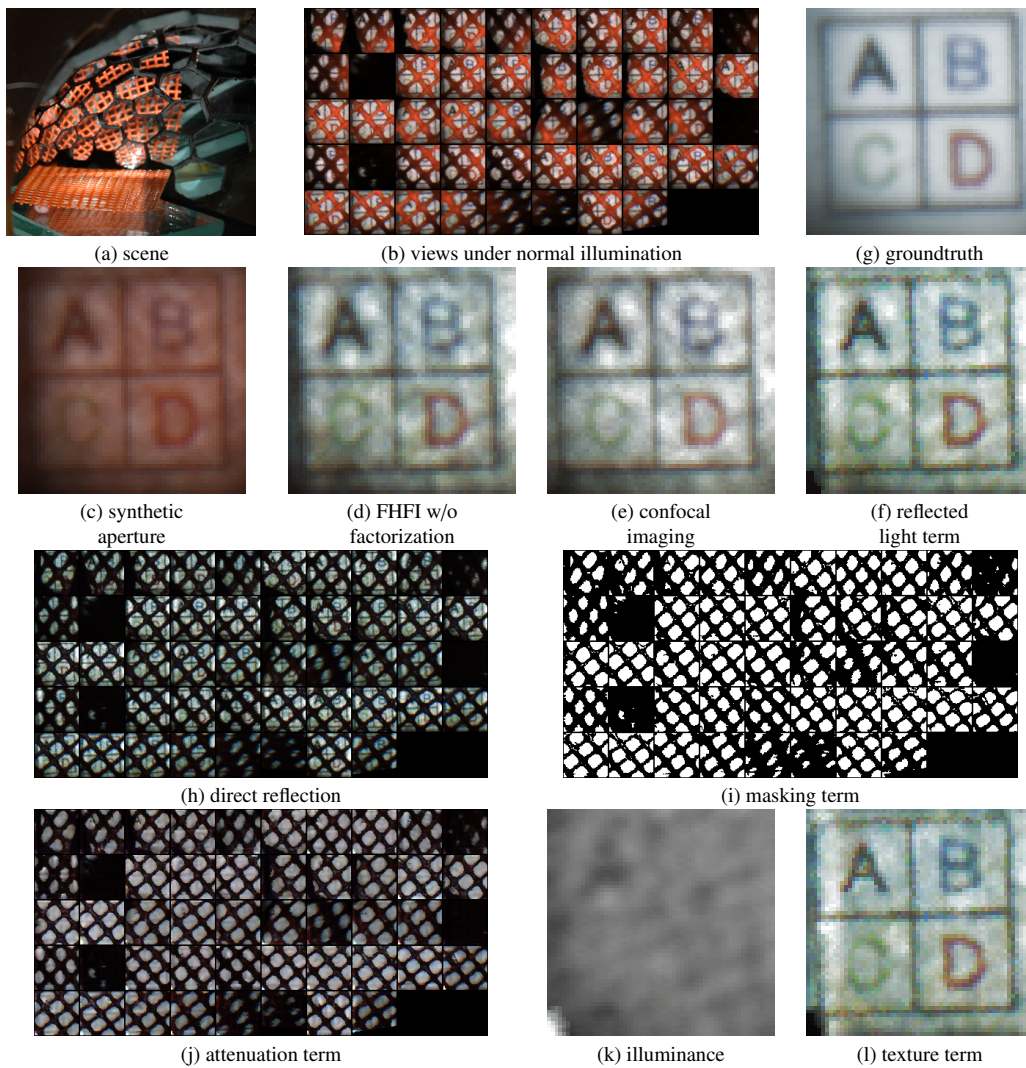


Fig. 24 Result of the combination of the FHFI and the factorization with an occluded scene.

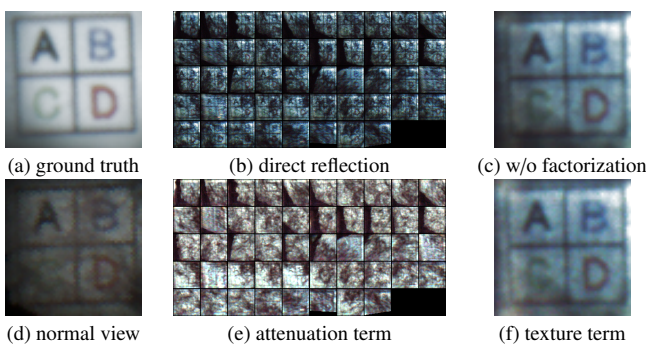


Fig. 25 Result of the combination of the FHFI and the factorization with an absorbed scene.

6.4 Limitations

- The resolution of the virtual projectors and cameras is low, because the imaging areas of the real projectors and cameras are divided into the virtual areas.
- The observable area is narrow because all of the projectors must illuminate and all of the cameras must observe a common area. To enlarge the area, a large turtleback reflector is necessary, and it may be difficult to construct.
- The factorization is basically an ill-posed problem. For example, we cannot distinguish between two different scenes

in which a red texture is covered with a colorless film and a white texture is covered with a red film. Some empirical constraints such as the smoothness of attenuation are necessary.

7. Conclusion

In this paper, we addressed the difficulty in using 8-D reflectance fields as imaging components because of the high dimensionality. So far, 8-D reflectance fields are well known as carrying useful information that can represent appearances of a target scene under varying illumination. Ideally, with 8-D reflectance fields we can create an image of a scene under arbitrary illumination in an arbitrary focus and viewpoint.

Here, we proposed fundamental techniques for imaging using 8-D reflectance fields. The fundamental techniques are how to measure, how to compute, and how to image. For how to measure, we designed the turtleback reflector. For how to compute, we established a unified framework for computing 8-D reflectance fields. For how to image, we developed the hemispherical confocal imaging as an example of an application analyzing a 8-D reflectance field.

Ultimately, although the techniques for 8-D reflectance fields

have not been addressed, by these proposed techniques, use of 8-D reflectance fields has become feasible and practical for various applications. We have made guidelines about how to use 8-D reflectance fields for imaging.

Acknowledgments This research is granted by the Japan Society for the Promotion of Science (JSPS) through the “Funding Program for Next Generation World-Leading Researchers (NEXT Program),” initiated by the Council for Science and Technology Policy (CSTP).

References

[1] Adelson, E. H. and Wang, J. Y.: Single Lens Stereo with a Plenoptic Camera, *IEEE Tran. on PAMI*, pp. 99–106 (1992).

[2] Candès, E. and Romberg, J.: Quantitative robust uncertainty principles and optimally sparse decompositions, Vol. 6(2), pp. 227–254 (2006).

[3] Candès, E., Romberg, J. and Tao, T.: Robust uncertainty principles: Exact signal reconstruction from highly incomplete frequency information, Vol. 52(2), pp. 489–509 (2006).

[4] Cossairt, O., Nayar, S. K. and Ramamoorthi, R.: Light Field Transfer: Global Illumination Between Real and Synthetic Objects (2008).

[5] Dana, K. J. and Wang, J.: Device for convenient measurement of spatially varying bidirectional reflectance, *J. Opt. Soc. Am. A*, Vol.21, Issue 1, pp. 1–12 (2004).

[6] Debevec, P., Hawkins, T., Tchou, C., Duiker, H.-P., Sarokin, W. and Sagar, M.: Acquiring the Reflectance Field of a Human Face, *Proc. SIGGRAPH2000*, pp. 145–156 (2000).

[7] Donoho, D.: Compressed sensing, *IEEE Transactions on Information Theory*, Vol. 52(4), pp. 1289–1306 (2006).

[8] Fuchs, C., Heinz, M., Levoy, M., Seidel, H.-P. and Lensch, H. P. A.: Combining Confocal Imaging and Descattering, *Computer Graphics Forum, Special Issue for the Eurographics Symposium on Rendering 2008*, Vol. 27, No. 4, pp. 1245–1253 (2008).

[9] Garg, G., Talvala, E.-V., Levoy, M. and Lensch, H. P. A.: Symmetric Photography : Exploiting Data-sparseness in Reflectance Fields, *Proc. EGSR2006*, pp. 251–262 (2006).

[10] Ghosh, A., Achutha, S., Heidrich, W. and O’Toole, M.: BRDF Acquisition with Basis Illumination, *Proc. ICCV2007* (2007).

[11] Gu, J., Nayar, S. K., Grinspun, E., Belhumeur, P. and Ramamoorthi, R.: Compressive Structured Light for Recovering Inhomogeneous Participating Media, *Proc. ECCV2008*, pp. 845–858 (2008).

[12] Kim, J., Horstmeyer, R., Kim, I.-J. and Raskar, R.: Highlighted Depth-of-Field Photography: Shining Light on Focus, *ACM Transactions on Graphics*, Vol. 30, No. 3 (2011).

[13] Kim, J., Lanman, D., Mukaigawa, Y. and Raskar, R.: Descattering Transmission via Angular Filtering, *Proc. ECCV2010*, pp. 86–99 (2010).

[14] Kusumoto, N., Hiura, S. and Sato, K.: Uncalibrated Synthetic Aperture for Defocus Control, *Proc. CVPR2009* (2009).

[15] Lanman, D., Raskar, R. and Taubin, G.: Modeling and Synthesis of Aperture Effects in Cameras, *Proc. Computational Aesthetics 2008: Eurographics Workshop (CAe2008)* (2008).

[16] Levin, A., Fergus, R., Durand, F. and Freeman, W. T.: Image and Depth from a Conventional Camera with a Coded Aperature, *Proc. SIGGRAPH2007* (2007).

[17] Levin, A., Hasinoff, S. W., Green, P., Durand, F. and Freeman, W. T.: 4D Frequency Analysis of Computational Cameras for Depth of Field Extension, *Proc. SIGGRAPH2009* (2009).

[18] Levoy, M., Chen, B., Vaish, V., Horowitz, M., McDowall, I. and Bolas, M.: Synthetic Aperture Confocal Imaging, *Proc. SIGGRAPH2004*, pp. 825–834 (2004).

[19] Levoy, M. and Hanrahan, P.: Light Field Rendering, *Proc. SIGGRAPH’96*, pp. 31–42 (1996).

[20] Li, H., Foo, S.-C., Torrance, K. E. and Westin, S. H.: Automated three-axis gonioreflectometer for computer graphics applications, *Optical Engineering*, Vol. 45(4) (2006).

[21] Masselus, V., Peers, P. and Dutré, P.: Relighting with 4D Incident Light Fields, *Proc. SIGGRAPH2003*, pp. 613–620 (2003).

[22] Matusik, W., Pfister, H., Ngan, A., Beardsley, P., Ziegler, R. and McMillan, L.: Image-Based 3D Photography using Opacity Hulls, *Proc. SIGGRAPH2002*, pp. 427–437 (2002).

[23] Minsky, M.: Microscopy Apparatus, US Patent 3013467 (1961).

[24] Mukaigawa, Y., Sumino, K. and Yagi, Y.: High-Speed Measurement of BRDF using an Ellipsoidal Mirror and a Projector, *Proc. IEEE International Workshop on Projector-Camera Systems (PRO-CAMS2007)* (2007).

[25] Mukaigawa, Y., Sumino, K. and Yagi, Y.: Multiplexed Illumination for Measuring BRDF using an Ellipsoidal Mirror and a Projector, *Proc. of Asian Conference on Computer Vision (ACCV2007)*, pp. 246–257 (2007).

[26] Müller, G., Bendels, G. H. and Klein, R.: Rapid Synchronous Acquisition of Geometry and Appearance of Cultural Heritage Artefacts, *The 6th International Symposium on Virtual Reality, Archaeology and Cultural Heritage (VAST)*, pp. 13–20 (2005).

[27] Narasimhan, S. G., Nayar, S. K., Sun, B. and Koppal, S. J.: Structured Light in Scattering Media, *Proc. ICCV2005, Vol 1*, pp. 420–427 (2005).

[28] Nayar, S. K., Krishnan, G., Grossberg, M. D. and Raskar, R.: Fast Separation of Direct and Global Components of a Scene using High Frequency Illumination, *Proc. SIGGRAPH2006*, pp. 935–944 (2006).

[29] Ng, R., Levoy, M., Brédif, M., Duval, G., Horowitz, M. and Hanrahan, P.: Light Field Photography with a Hand-held Plenoptic Camera, *Stanford Tech Report CTSR 2005-02* (2005).

[30] Peers, P. and Dutré, P.: Inferring Reflectance Functions from Wavelet Noise, *Proc. the 16th Eurographics Symposium on Rendering*, pp. 173–182 (2005).

[31] Peers, P., Mahajan, D., Lamond, B., Ghosh, A., Matusik, W., Ramamoorthi, R. and Debevec, P.: Compressive Light Transport Sensing, *ACM Transactions on Graphics* (2009).

[32] Raskar, R., Agrawal, A. and Tumblin, J.: Coded Exposure Photography: Motion Deblurring using Fluttered Shutter, *ACM SIGGRAPH 2006* (2006).

[33] Sato, I., Okabe, T., Sato, Y. and Ikeuchi, K.: Appearance Sampling for Obtaining a Set of Basis Images for Variable Illumination, *Proc. ICCV2003*, pp. 800–807 (2003).

[34] Sen, P., Chen, B., Garg, G. and Marschner, S. R.: Dual Photography, *Proc. SIGGRAPH2005*, pp. 745–755 (2005).

[35] Tagawa, S., Mukaigawa, Y., Kim, J., Raskar, R., Matsushita, Y. and Yagi, Y.: Hemispherical Confocal Imaging, *IP SJ Transactions on Computer Vision and Applications*, Vol. 3, pp. 222–235 (2011).

[36] Treibitz, T. and Schechner, Y. Y.: Active Polarization Descattering, pp. 385–399 (2009).

[37] Unger, J., Wenger, A., Hawkins, T. C., Gardner, A. and Debevec, P.: Capturing and Rendering With Incident Light Fields.

[38] Vaish, V., Szeliski, R., Zitnick, C. L. and Kang, S. B.: Reconstructing Occluded Surfaces using Synthetic Apertures: Stereo, Focus and Robust Measures, *CVPR2006, Vol.II*, pp. 2331–2338 (2006).

[39] Vaish, V., Wilburn, B., Joshi, N. and Levoy, M.: Using Plane + Parallax for Calibrate Dense Camera Arrays, *Proc. CVPR 2004* (2004).

[40] Veeraraghavan, A., Raskar, R., Agrawal, A., Mohan, A. and Tumblin, J.: Dappled Photography: Mask Enhanced Cameras for Heterodyned Light Fields and Coded Aperture Refocusing, *Proc. SIGGRAPH2007* (2007).

[41] Ward, G. J.: Measuring and Modeling Anisotropic Reflection, *Proc. SIGGRAPH’92*, pp. 255–272 (1992).

[42] Wilburn, B., Joshi, N., Vaish, V., Talvala, E.-V., Antunez, E., Barth, A., Adams, A., Horowitz, M. and Levoy, M.: High Performance Imaging Using Large Camera Arrays, *Proc. SIGGRAPH2005*, pp. 765–776 (2005).